Magnetic Resonance in Medicine 74:647–660 (2015)

Real-Time Motion Correction Using Gradient Tones and Head-Mounted NMR Field Probes

Maximilian Haeberlin,[1] Lars Kasper,[1,2] Christoph Barmet,[1,3] David O. Brunner,[1] Benjamin E. Dietrich,[1] Simon Gross,[1] Bertram J. Wilm,[1] Sebastian Kozerke,[1] and Klaas P. Pruessmann[1]*

Purpose: Sinusoidal gradient oscillations in the kilohertz range are proposed for position tracking of NMR probes and prospective motion correction for arbitrary imaging sequences without any alteration of sequence timing. The method is combined with concurrent field monitoring to robustly perform image reconstruction in the presence of potential dynamic field deviations.

Methods: Benchmarking experiments were done to assess the accuracy and precision of the method and to compare it with theoretical predictions based on the field probe's time-dependent signal-to-noise ratio. An array of four field probes was used to perform real-time prospective motion correction in vivo. Images were reconstructed based on both predetermined and concurrently measured k-space trajectories.

Results: For observation windows of 4.8 ms, the precision of probe position determination was found to be 35 to 62 μm, and the maximal measurement error was 595 μm root-mean-square on a single axis. Sequence update per repetition time on this basis yielded images free of conspicuous artifacts despite substantial head motion. Predetermined and concurrently observed k-space trajectories yielded equivalent image quality.

Conclusion: NMR field probes in conjunction with gradient tones permit the tracking and prospective correction of rigid-body motion. Relying on gradient oscillations in the kilohertz range, the method allows for concurrent motion detection and image encoding. **Magn Reson Med 74:647–660, 2015. © 2014 Wiley Periodicals, Inc.**

Key words: field monitoring; prospective; position tracking; head motion; external; marker

INTRODUCTION

During an MRI examination, patients often move for reasons including discomfort, restlessness, nervousness, or pain. Such motion can cause various image artifacts such as ghosting, blurring, and ringing, and also erroneous quantification of anatomical and physiological properties such as diffusion parameters, tissue volumes, and blood-oxygen-level-dependent activation (1,2). Motion hampers the application of MR to large groups of subjects with difficulty to keep still such as children, seniors, and patients with neurological conditions. Even in compliant subjects, involuntary motion still limits imaging accuracy (3) and achievable resolution and can be exacerbated in functional MRI (fMRI) with certain paradigms such as motor tasks (4–6).

Upon image reconstruction, motion can be accounted for retrospectively based on different estimation methods (7,8) that have been applied to correct for cardiac (9–11), respiratory (12,13), head, and shoulder motion. However, retrospective motion correction fails in the case of inconsistent selective excitation, which results in image artifacts or slice misalignment; and it also fails in the case of signal dropouts, which are problematic in diffusion-weighted imaging, for example. To overcome these problems, the imaging sequence needs to be dynamically adjusted based on information about the motion state. Such information is challenging to retrieve and utilized for nonrigid motion patterns such as those encountered in the heart and abdomen. However, it is more amenable for rigid-body motion such as that of the head, which can be parameterized with few degrees of freedom and readily addressed by the reorientation of imaging gradients and the adjustment of excitation and demodulation frequencies (14).

Early approaches for tracking head position were reported in (15,16) based on the navigator technique proposed in (17). Extensions thereof to two and three dimensions led to the development of orbital, spherical, and cloverleaf navigators (18–20). One downside to navigator techniques, however, is that they require additional sequence modules, which constrain contrast optimization and increase overall scan duration, particularly for short-repetition time (TR) sequences that are widely used in clinical practice. Furthermore, by relying on MR signal from the head itself, navigators may alter the magnetization state of tissue to be imaged, which additionally complicates sequence design.

Interference with tissue magnetization can be overcome by external NMR markers based on small samples in miniature radio-frequency (RF) coils (21,22), as originally proposed for catheter tracking (23). However, these methods still require a sequence overhead and additional scan time because they rely on a localization module applied between imaging readouts (24,25).

[1]Institute for Biomedical Engineering, University of Zurich and ETH Zurich, Zurich, Switzerland.
[2]Translational Neuromodeling Unit, Institute for Biomedical Engineering, University of Zurich and ETH Zurich, Zurich, Switzerland.
[3]Skope Magnetic Resonance Technologies, Zurich, Switzerland.

*Correspondence to: Klaas P. Pruessmann, Institute for Biomedical Engineering, University and ETH Zurich, Gloriastrasse 35, 8092 Zurich, Switzerland. E-mail: pruessmann@biomed.ee.ethz.ch

M.H. was funded by a National Competence Center for Biomedical Imaging (NCCBI) PhD fellowship from the Swiss NCCBI. C.B. was supported by ETH Zurich with a Pioneer Fellowship. D.B. received financial support from the Hans-Eggenberger-Stiftung through a Hans-Eggenberger-Prize Grant.

Received 17 March 2014; revised 30 July 2014; accepted 7 August 2014

DOI 10.1002/mrm.25432

Published online 12 September 2014 in Wiley Online Library (wileyonlinelibrary.com).

Interference with sequence design has been overcome with optical motion tracking (26–28) by means of a camera attached to the head in order to observe a marker. Implementations of this concept have been proposed using different types of markers, such as self-encoded checkerboard markers (27,29), retroreflective markers (26), and retrograde reflective moiré patterns (28), as well as different camera locations inside (3,27) and outside the magnet bore (26,28). Optical motion tracking works independently of the MR experiment and thus demands neither sequence alterations and scan time overhead nor any manipulation of tissue magnetization. Unlike current NMR marker approaches, it permits motion detection during arbitrary time windows. A remaining drawback of optical motion tracking, however, is that it requires line-of-sight access to the marker, which can interfere with other demands such as tight-fitting receiver arrays or fMRI equipment such as mirrors or goggles.

The goal of the present work is to reconcile the advantages of the aforementioned approaches while avoiding their individual limitations. To this end, we revert to the concept of position tracking with external NMR probes, yet avoid sequence overhead and timing issues. This is achieved by the use of high-sensitivity ^{19}F NMR probes localized by gradient tones (i.e., high-frequency gradient oscillations), which are superimposed to a given sequence without affecting its timing. Tones of different frequency are played out via each gradient coil to establish a unique relationship between the position of a probe and the amplitudes of its respective signal phase modulations. High tone frequencies in the kilohertz range are used to achieve robustness against thermal, physiological, and ambient field fluctuations and to preserve effective image encoding. In this way, the localization and imaging tasks are separated in the frequency domain rather than in time, which permits their simultaneous execution.

Spectral separation also enables continuous field-probe localization and is not limited to certain sequence windows. In particular, freedom of probe timing permits exactly simultaneous acquisition of probe and imaging signals. This option is of added interest because it promises utility beyond mere prospective sequence adjustment. When operating head-mounted NMR probes simultaneously with periods of image data acquisition, they capture not only position information encoded via the gradient tones but also all other field dynamics that contribute to image encoding. These include potential low-frequency perturbations such as thermal drifts, gradient delays, eddy current effects, and field fluctuations due to breathing. Such effects have previously been accounted for by field monitoring with sets of NMR probes mounted in the MR system (30–32). However, they can equally be extracted from head-mounted probes, which then effectively act as a field monitoring system in the head frame of reference. Conveniently, in the head frame of reference, any motion during imaging readouts will appear just as an additional distortion of the field evolution. Therefore, the signals of head-mounted probes form a powerful basis not only on between-TR motion tracking but also of image reconstruction, for which they permit accounting for both low-frequency field imperfections and residual within-TR motion.

To assess the proposed method in terms of localization precision and accuracy, it is first used for tracking of a single probe. In the second part of the study, it is then employed for prospective motion correction in brain imaging, using a T_1-weighted gradient-echo sequence in vivo. The potential utility of within-TR field monitoring is tested by comparing image reconstruction based on either the monitoring information or a predetermined reference trajectory.

METHODS

Probe Tracking with Gradient Tones

The basic concept pursued in this work is to track magnetic field probes by reliable and reproducible gradient field evolutions that do not alter characteristics of the MR imaging sequence, such as the field of view and the resolution. Requirements on a suitable gradient waveform for probe tracking include the ability to uniquely encode coordinates in all three spatial dimensions within an arbitrarily placed, narrow time window; an easy response characterization; and robustness to external field contaminations. Furthermore, the position-encoding gradient waveform should impose small moments onto image encoding trajectories and be easily separable from typical MR gradient sequences.

Sinusoidal gradient waveforms at kilohertz frequencies meet all these requirements. Operated in parallel at different frequencies on each of the three gradient coils, they are able to encode all three spatial coordinates synchronously and within arbitrary time windows. It is preferable to choose high oscillation frequencies because it improves the separation between the sinusoids and most common field contaminations, which occur at lower frequencies (e.g., main magnetic field drifts and local field variations due to motion of magnetized tissue). Moreover, gradient system behavior at high frequencies is more stable over time. Being eigenfunctions of linear time invariant systems, sinusoids can be readily characterized in terms of gain, delay, and coupling behavior. The accessible band for sinusoidal gradient tones is lower-bounded by the significant bandwidth of the gradient sequence waveforms and upper-bounded by the gradient system's bandwidth, suggesting frequencies of 5 to 15 kHz on common gradient systems. A triplet of such gradient tones can be formalized as follows:

$$\boldsymbol{G}_{tone}(t) = \left[A_x \sin(2\pi f_x t),\ A_y \sin\left(2\pi f_y t\right),\ A_z \sin(2\pi f_z t)\right], \quad [1]$$

where A_l denotes the amplitude of the tone along the spatial dimension l, f_i its frequency, and t denotes time.

Determination of Probe Position

The tones-encoded spatial coordinates of an NMR field probe can be obtained from its phase evolution, which is retrieved by unwrapping the demodulated probe signal (30). The underlying field evolution is given by the temporal derivative of the probe phase,

$$\frac{1}{\gamma}\frac{\mathrm{d}\phi(t)}{\mathrm{d}t} = B(t) = \boldsymbol{G}_{tone}(t)\boldsymbol{r} + B_0(\boldsymbol{r}) + \eta(t), \quad [2]$$

where $B(t)$ denotes the measured magnetic field at the probe's position $\boldsymbol{r}$, $B_0(\boldsymbol{r})$ denotes the static magnetic field at that position, and motion during the probe readout is neglected. t denotes time, and $\eta(t)$ denotes real-valued additive Gaussian noise. $\phi(t)$ denotes the unwrapped phase of the demodulated probe signal, as described in (31), and γ denotes the gyromagnetic ratio of the field probe's NMR active sample. The noise level of the field measurement depends on the probe signal's time-dependent signal-to-noise ratio (SNR), which is limited by thermal noise in the field probe's receive chain.

Assembling the sampled field values in the column vector $\boldsymbol{b}$, the field model can be written in matrix-vector notation:

$$\boldsymbol{b} = \boldsymbol{G}_{tone}\boldsymbol{r} + \mathbf{1}B_0(\boldsymbol{r}) + \boldsymbol{\eta}, \quad [3]$$

where $\boldsymbol{G}_{tone}$ is a matrix whose elements (n, l) denote gradient field values along the spatial dimension $l = x, y, z$ sampled at $t = n\Delta t$. The sampling interval is denoted by Δt, and n is an integer counting the samples. $\mathbf{1}$ is a column vector filled with ones, and $\boldsymbol{\eta}$ is the vector of sampled noise instances. $\boldsymbol{\eta}$ is of zero mean, and time-dependent signal standard deviation $\sigma_b(n\Delta t) = 1/(\gamma\Delta t\ SNR(n\Delta t))$, where $SNR(n\Delta t)$ denotes the SNR of the complex-valued probe signal and γ denotes the gyromagnetic ratio of the probe's nucleus. $\boldsymbol{\Psi}_b$ denotes the covariance matrix of $\boldsymbol{\eta}$ with diagonal elements $\boldsymbol{\Psi}_b(n, n) = \sigma_b^2(n\Delta t)$. A more detailed derivation of the noise statistics is given in (31).

The probe's coordinates can be obtained in two steps. First, $\boldsymbol{b}$ is projected onto the subspace spanned by the tones:

$$\boldsymbol{G}_{tone}{}^H\boldsymbol{b} = \boldsymbol{G}_{tone}{}^H\boldsymbol{G}_{tone}\boldsymbol{r} + \boldsymbol{G}_{tone}{}^H\mathbf{1}B_0(\boldsymbol{r}), \quad [4]$$

which reduces to the following normal equation:

$$\boldsymbol{G}_{tone}{}^H\boldsymbol{b} = \boldsymbol{G}_{tone}{}^H\boldsymbol{G}_{tone}\boldsymbol{r} \quad [5]$$

under the constraint:

$$\boldsymbol{G}_{tone}{}^H\mathbf{1} = 0. \quad [6]$$

The superscript H is the hermitian adjoint operator. Eq. [6] requires the gradient tone waveform to be of zero mean in the designated time window, which renders position determination independent of the static field. This requirement is fulfilled by small adjustments of the tone frequencies such that they are harmonics of the probe signal's acquisition window. In a second step, the SNR-optimal least-squares estimate of $\boldsymbol{r}$ is obtained by

$$\boldsymbol{r} = \boldsymbol{G}_{tone}{}^+\boldsymbol{b}, \quad [7]$$

where $\boldsymbol{G}_{tone}{}^+ = \left(\boldsymbol{G}_{tone}{}^H\boldsymbol{\Psi}_\mathrm{b}{}^{-1}\boldsymbol{G}_{tone}\right)^{-1}\boldsymbol{G}_{tone}{}^H\boldsymbol{\Psi}_\mathrm{b}{}^{-1}$ denotes the SNR-optimal Moore-Penrose pseudoinverse of $\boldsymbol{G}_{tone}$.

The precision of the position measurement can be formalized as follows:

$$\boldsymbol{\Psi}_r = \boldsymbol{G}_{tone}{}^+\boldsymbol{\Psi}_b(\boldsymbol{G}_{tone}{}^+)^H = \left(\boldsymbol{G}_{tone}{}^H\boldsymbol{\Psi}_\mathrm{b}{}^{-1}\boldsymbol{G}_{tone}\right)^{-1}, \quad [8]$$

$$\sigma_{r_i}^2 = (\boldsymbol{\Psi}_r)_{i,i}, \quad [9]$$

where $\boldsymbol{\Psi}_r$ denotes the noise covariance matrix, and $\sigma_{r_i}^2$ is the variance of the probe coordinate $\mathbf{r}_i$. Eqs. [8] and [9] allow predicting the precision of the position measurement based on its time-dependent SNR.

Gradient Response and Calibration

The considerations above assume ideal gradient performance. To account for real gradient behavior, the field response of a tone was modeled as the output of a linear time-invariant (LTI) system, encompassing linear effects such as amplitude scaling, phase delays, and coupling into other field components. The LTI behavior of the gradient system could be determined by measuring its full impulse response function (33). In this work, however, it is sufficient to know that the system response at the three tone frequencies and a full LTI characterization via the impulse response function were not required. Instead, the tones were formalized as complex exponentials, changing Eq. [1] as follows:

$$\boldsymbol{G}_{tone}(t) = \left[\, A_x e^{i2\pi f_x t}, \quad A_y e^{i2\pi f_y t}, \quad A_z e^{i2\pi f_z t} \,\right], \quad [10]$$

The system response was modeled as a multiplication with the complex-valued matrix $(\boldsymbol{C}|\boldsymbol{c}_0)$, which augments Eq. [3] as follows:

$$\boldsymbol{b} = \boldsymbol{G}_{tone}(\boldsymbol{C}|\boldsymbol{c}_0)\begin{pmatrix}\boldsymbol{r}\\ 1\end{pmatrix} + \mathbf{1}B_0(\boldsymbol{r}), \quad [11]$$

where $\boldsymbol{C}$ denotes a complex-valued 3×3 matrix with elements $c_{m,l}$ reflecting the coupling between the applied tone at a frequency f_m and a gradient field component on the l axis. $\boldsymbol{c}_0$ denotes a column vector of coupling factors $c_{m,0}$ from the applied tones to the homogeneous field component, and m denotes the frequency index. If one chooses to neglect coupling between different field components, $\boldsymbol{C}$ becomes diagonal and $\boldsymbol{c}_0$ vanishes. Analogously to Eq. [7], the probe positions are obtained by a linear inversion of Eq. [11]:

$$\boldsymbol{r} = \boldsymbol{C}^+(\boldsymbol{G}_{tone}{}^+\boldsymbol{b} - \boldsymbol{c}_0). \quad [12]$$

Note that the term $\mathbf{1}B_0(\boldsymbol{r})$ vanishes under the constraint described by Eq. [6] and that the position obtained in this way is generally complex, whereas a real value is expected from the physical model in Eq. [2]. Given perfect decoupling, it is sufficient to consider the real part of $\boldsymbol{r}$ as the probe's position. In order to be robust against small variations in the tones phase, however, it is also possible to consider the magnitude of $\boldsymbol{r}$ as the probe's position, with the real part of $\boldsymbol{r}$ determining the sign of the position. In this work, the latter method was used to obtain the probe's position.

The individual rows of the system response matrix $(\boldsymbol{C}|\boldsymbol{c}_0)$ can be obtained by measuring tones responses at four known positions $\boldsymbol{r}_{1\text{–}4}$, yielding a modification of Eq. [11] as follows:

$$(\boldsymbol{b}_1, \boldsymbol{b}_2, \boldsymbol{b}_3, \boldsymbol{b}_4) = \boldsymbol{G}_{tone}(\boldsymbol{C}|\boldsymbol{c}_0)\begin{pmatrix} \boldsymbol{r}_1 & \boldsymbol{r}_2 & \boldsymbol{r}_3 & \boldsymbol{r}_4 \\ 1 & 1 & 1 & 1 \end{pmatrix} + \mathbf{1}(B_0(\boldsymbol{r}_1), B_0(\boldsymbol{r}_2), B_0(\boldsymbol{r}_3), B_0(\boldsymbol{r}_4)). \quad [13]$$

The least-squares estimate of the matrix $(\boldsymbol{C}|\boldsymbol{c}_0)$ is obtained by linear algebra:

$$\boldsymbol{G}_{tone}{}^{+}(\boldsymbol{b}_1, \boldsymbol{b}_2, \boldsymbol{b}_3, \boldsymbol{b}_4)\begin{pmatrix} \boldsymbol{r}_1 & \boldsymbol{r}_2 & \boldsymbol{r}_3 & \boldsymbol{r}_4 \\ 1 & 1 & 1 & 1 \end{pmatrix}^{-1} = (\boldsymbol{C}|\boldsymbol{c}_0), \quad [14]$$

where the last term in Eq. [13] again drops out due to condition [6].

Prospective Rigid-Body Motion Correction

The capability to localize NMR field probes enables the position tracking of the head if at least three such probes are attached to it in a linearly independent, rigid-body configuration (24). In order to both track the head orientation with 6 degrees of freedom and perform field monitoring of 0th and 1st order, a rigid body arrangement of four NMR field probes is required.

The first objective is to track the positions of the probes during arbitrary MR gradient activity. The superposition of tones and other sequence gradient waveforms causes field evolutions not captured in Eq. [3], which needs to be augmented as follows:

$$\boldsymbol{b} = (\boldsymbol{G}_{sequence} + \boldsymbol{G}_{tone})\boldsymbol{r} + \mathbf{1}B_0(\boldsymbol{r}), \quad [15]$$

where $\boldsymbol{G}_{sequence}$ is a matrix whose elements (k, l) denote gradient field values along the spatial dimension l sampled at $t = k\Delta t$. The recovery of the probes positions is achieved under an additional constraint,

$$\boldsymbol{G}_{tone}{}^{H}\boldsymbol{G}_{sequence} = 0, \quad [16]$$

which requires that the tones be orthogonal to the imaging sequence's original gradient waveforms. To estimate $\boldsymbol{r}$ from Eq. [15], it is first left multiplied by $\boldsymbol{G}_{tone}{}^{H}$, resulting in the elimination of two terms according to Eqs. [6] and [16], and then solved for $\boldsymbol{r}$:

$$\boldsymbol{r} = \boldsymbol{G}_{tone}{}^{+}\boldsymbol{b}, \quad [17]$$

where $\boldsymbol{G}_{tone}{}^{+} = \left(\boldsymbol{G}_{tone}{}^{H}\boldsymbol{G}_{tone}\right)^{-1}\boldsymbol{G}_{tone}{}^{H}$ denotes the Moore-Penrose pseudoinverse of $\boldsymbol{G}_{tone}$. Note that Eq. [17] differs from Eq. [7] in that it does not apply $\boldsymbol{\Psi}_{\mathrm{b}}{}^{-1}$ to optimize SNR, which would otherwise violate Eq. [16].

The orthogonality between foreground gradient activity and the tones can be achieved in various ways, for example, by band-stop filtering the sequence gradient waveforms in the frequency domain around the tones frequencies. For optimal use of the gradient system capabilities, gradient tones need to be codesigned with the temporally overlapping gradient waveforms (Fig. 1). System characteristics such as maximum gradient strength, slew rate, and bandwidth need to be met jointly. In the present work, a spin-warp sequence was chosen for the image encoding and modified to incorporate three gradient tones at frequencies $f_x = 6\ kHz$, $f_y = 7\ kHz$, and $f_z = 8\ kHz$, with identical nominal amplitudes $A_x = A_y = A_z = 3.71\ mT/m$. In order to superimpose the tones within gradient specifications, the initial waveform's maximum gradient strength and slew rate were $19\ mT/m$ and $40\ mT/m/ms$, respectively, values well below the gradient system limitations of $31\ mT/m$ and $200\ mT/m/ms$. In a second step, the waveform was band-stop filtered using MATLAB Release 2010a (MathWorks, Inc., Natick, MA). The band-stop filter was obtained in an equiripple, finite-impulse response filter design using the MATLAB implementation of the Parks-McClellan algorithm. The desired tones frequencies were adjusted slightly $(10 - 70\ Hz)$ to make them harmonics of the acquisition window and fulfill Eq. [6].

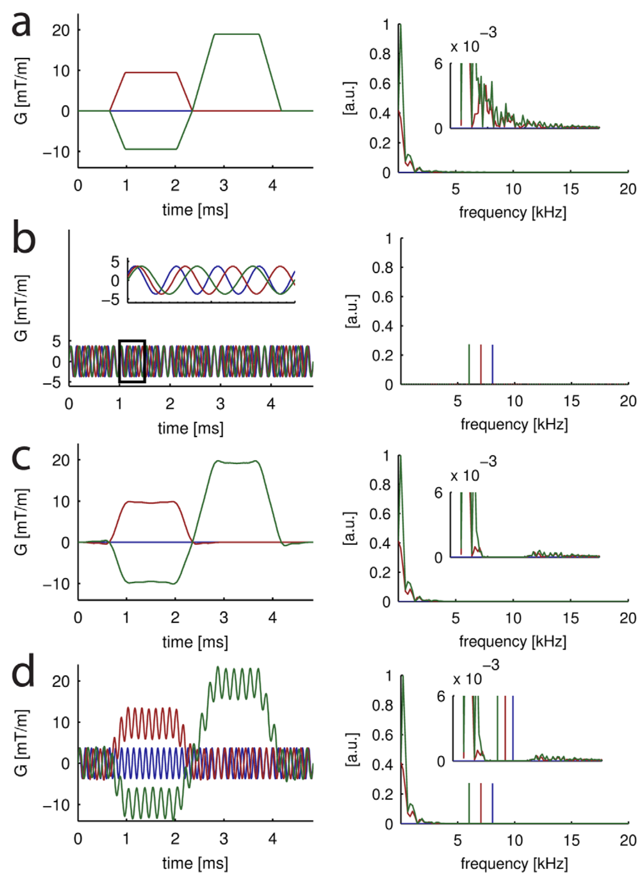

FIG. 1. Co-design of the image encoding waveform and gradient tones. (**a**) The starting point is the choice of the image-encoding waveform, a spin-warp in this case. (**b**) In a second step, three different frequencies are selected for the gradient tones. The choice has to consider the gradient system's transfer function, which linearly affects the method's sensitivity. (**c**) In a third step, the spectrum of the image encoding waveform is filtered at or around the tones frequencies to orthogonalize the image encoding from the tones. To minimize the filter's effect on the image encoding in the time domain, it is beneficial for the gradient tones to lie in spare bands of the image encoding gradients' spectrum. The superposition of the two is depicted in (**d**). The resulting waveform is capable of synchronously performing MR image encoding as well as field probe localization.

A closed-form solution for the rotation and translation parameters, $\boldsymbol{R}$ and $\boldsymbol{t}$, was derived by Umeyama (34). It yields the optimal (in the least-squares sense) rotation and translation parameters considering the covariance between a set of updated probe positions and a set of reference coordinates:

$$\boldsymbol{R} = \boldsymbol{USV}^T, \boldsymbol{t} = \boldsymbol{m}_y - \boldsymbol{Rm}_x, \quad [18]$$

with

$$\boldsymbol{m}_y = \frac{1}{N}\sum_{i=1}^{N}\boldsymbol{y}_i, \boldsymbol{m}_x = \frac{1}{N}\sum_{i=1}^{N}\boldsymbol{x}_i, \quad [19]$$

$$\boldsymbol{UDV}^T = \frac{1}{N}\sum_{i=1}^{N}(\boldsymbol{y}_i - \boldsymbol{m}_y)(\boldsymbol{x}_i - \boldsymbol{m}_x)^T, \quad [20]$$

$$\boldsymbol{S} = \begin{cases} diag(1,1,1) & if \det\left(\boldsymbol{UDV}^T\right) \geq 0 \\ diag(1,1,-1) & if \det\left(\boldsymbol{UDV}^T\right) < 0 \end{cases} \quad [21]$$

where $\boldsymbol{R}$ and $\boldsymbol{t}$ denote the rotation matrix and the translation vector that map the updated positions $\boldsymbol{y}_1, \ldots, \boldsymbol{y}_N$ of N field probes to a set of reference positions $\boldsymbol{x}_1, \ldots, \boldsymbol{x}_N$. $\boldsymbol{UDV}^T$ is the result of the singular value decomposition of the position covariance matrix.

The field probe data were processed directly on the MR system's spectrometer. Immediately after each data acquisition, the probes' positions were calculated according to Eq. [12] using the definition of $\boldsymbol{G}_{tone}{}^{+}$, as defined in Eq. [17] and compared to a set of reference coordinates obtained with gradient tones during the first interleave of the scan to determine the motion parameters, as defined in Eq. [18]. For prospective motion correction the sequence was locked to the patient frame of reference by rotating all gradient waveforms, including the gradient tones, and shifting the RF center frequency prior to each slice excitation.

NMR Field Probe Interface and Operation

All experiments were conducted using NMR field probes as described in (31,35). To avoid RF interference between the monitoring and the imaging experiment, perfluoropinacol-based ^{19}F NMR field probes were used with a droplet diameter of 1 *mm* and a Larmor frequency of 120.2 *MHz*. The probe sensitivity is reflected by the criterion ξ (31), which denotes the product of the probe SNR and the square root of the acquisition bandwidth. For the probes used in the motion correction experiment ($T_2^* = 4\ ms$), it amounted to $\xi = 7.9 \cdot 10^4\sqrt{Hz}$. The signal characteristics of the probe used in the benchmarking measurements were $T_2^* = 9\,ms$ and $\xi = 8.1 \cdot 10^4\sqrt{Hz}$. The field probes were connected to the spectrometer of a 3T Philips Achieva system, which was used for all experiments described in the following. The field probes were excited immediately before the start of the data acquisition with a hard excitation pulse (duration 5 μs; nutation frequency 50 *kHz*; power ≈ 5 *W*) triggered by separate hardware. The custom-built hardware interface included separate excitation chains, preamplifiers, and booster stages, as well as PIN diode switches for independent transmit–receive operation (36).

Data Acquisition

Gradient Response and Calibration

To obtain the coupling coefficients, a single NMR field probe was rigidly attached to a homemade acrylic-glass scaffold placed inside the bore of the MR system. The experiment consisted of 255 repetitions of a gradient sequence consisting of three synchronous tones and was performed for four different positions of the NMR field probe, forming approximately a tetrahedron. The tone frequencies were $f_x = 6\ kHz$, $f_y = 7\ kHz$, and $f_z = 8\ kHz$, with nominal amplitudes $A_x = A_y = A_z = 3.71\ mT/m$, The acquisition bandwidth was 439 *kHz*, the time window used for the localization was 4.8 *ms* and $T_R = 100\ ms$. The reference coordinates used in Eq. [13] were determined by measuring the field probes' NMR frequency shifts under static gradients of 2.5 mT/m in the x, y and z directions, respectively (23).

Performance of Probe Localization and Rigid-Body Tracking

To assess the performance of tone-based field probe localization and rigid-body tracking, accuracy and precision measurements were performed using the same experimental setup as for the gradient response calibration experiment. One field probe was placed at two opposing ends of the field of view (start and end position) and both tones-based localizations as well as reference position measurements were performed at each position using the same tones frequencies, amplitudes, acquisition bandwidth, TR and time window as in the previous experiment. The probe's reference coordinates were obtained by measuring its NMR frequency shift under three sequential static field gradients (23). The reference experiment was repeated 20 times for both positions in order to estimate its sensitivity as well as controlling for undesired minute probe displacements. Positions obtained from both methods were compared for consistency (root-mean-square discrepancy), and their precision (standard deviation [SD]) was computed. Additionally, the precision was predicted with Eq. [9]. The field probe was then moved by hand from the start to end position while the tones-based tracking sequence was running. Finally, the effect of field coupling on the tones-based localization was quantified by computing the probe coordinates with a purely diagonal system response matrix $\boldsymbol{C}$ and comparing them with probe coordinates computed using the full system response obtained in the previous experiment. The matrix elements used in this case were obtained from a single calibration measurement at the start position, as opposed to the four positions required for the previous case.

To estimate error in rigid-body tracking, the stationary calibration setup was used for 255 successive instances of determining translation and rotation parameters in the absence of motion.

Motion Correction Experiments

The field probe array was mounted on a pair of standard MR headphones to perform the prospective motion correction experiment. The only two modifications to the headphones were the removal of the housing around the ears to maximize freedom of motion and the attachment of a short beam orthogonal to the frame connecting the two sides (Fig. 2).

Both functions of the field probe array, field monitoring and determination of head orientation, are well conditioned if the field probes are placed at the vertices of a tetrahedron. The field probe arrangement was chosen accordingly. Comprising four field probes, the headphone setup can readily be used for gradient system response calibration when the headphone setup is stationary. This was achieved by rigidly placing it in the center of the MR system's field of view. Fixation was achieved by attaching the setup to a static spherical water phantom.

In the in vivo experiment, a healthy volunteer was equipped with the headphone setup and put into the MR system. In the phantom experiment, the head setup was taped to a structured water phantom that was rigidly placed inside the MR system. All experiments in this section, that is, the calibration, phantom, and motion correction experiments, were conducted using an 8-channel Philips SENSE head coil. An RF-spoiled, T_1-weighted multislice gradient echo sequence was chosen with the following parameters: field of view 23 *cm*, resolution 0.9 *mm*, 7 axial slices, slice thickness 5 *mm*, $TR = 40.1$ *ms*, flip angle 80°, and total imaging time $= 71$ *s*. The tones frequencies, amplitudes, acquisition bandwidth, and time window were identical those of the previous experiments.

Five phantom experiments were conducted: In the first phantom experiment, the setup was put in position 1 and the imaging sequence was played out twice, once with sequence update based on motion tracking and once without update to assess potential image artifacts induced by the tracking system. In the second phantom experiment, the sequence update was again suppressed and the imaging sequence was played out without the gradient tones to assess their potential impact on image quality. In the third phantom experiment, the imaging sequence, including tones, was played out without sequence update to obtain a reference trajectory for calibrated image reconstruction. In the fourth phantom experiment, the sequence update was performed during repeated imaging under the influence of motion. In the first repetition, an image was obtained while the setup was stationary at position 1. The phantom was rotated by hand about the z-axis to position 2 in the second repetition, followed by a third repetition in which a second image again was taken in stationary conditions. In the fifth phantom experiment, the setup was left stationary in position 2 and imaged without sequence update to illustrate the actual position change. Reference probe coordinates were acquired prior to the first phantom experiment for position 1 and after the fourth experiment for position 2.

Two in vivo experiments were carried out as follows: In the first experiment, the volunteer was asked to perform a head rotation around the magnet's main axis and then return to the initial position. In the second experiment, the volunteer was asked to perform a shift along the magnet's main axis orthogonal to the imaging slice, also returning to the initial position. Both scenarios were performed twice, with and without motion tracking, respectively.

Field Monitoring and Image Reconstruction

Dynamic magnetic fields of 0th and 1st spatial order were computed from the same field probe data as used for slice tracking, and a set of reference positions and static off-resonance frequencies was acquired at the beginning of the scan session. In the experiments with motion correction, 2D image reconstruction was conducted based on the concurrently monitored dynamic field data with an iterative conjugate-gradient algorithm using gridding. Note that the concurrently monitored dynamic fields are inherently measured in the subject's frame of reference. In the experiments without motion correction, image reconstruction was conducted based on a previously monitored k-space trajectory of 0th and 1st spatial order. Phase evolutions in the object caused by the tone orthogonal to the imaging slice were a function of the time-dependent off-center position of each slice and were taken into account throughout.

RESULTS

Gradient Response and Calibration

Table 1 shows the gradient system response matrix. The desired field components along each axis amounted to 0.66 (G_x, 6 *kHz*), 0.59 (G_y, 7 *kHz*), and 0.53 (G_z, 8 *kHz*), respectively. The cross-term magnitudes were naturally much smaller, ranging between $4.7 \cdot 10^{-4}$ and $6.9 \cdot 10^{-3}$. The phase values of the diagonal elements were determined with precisions around 0.014°. The phases of the small cross-terms could not be determined with high

FIG. 2. The motion correction setup as used in this work. It consists of an array of four ^{19}F NMR field probes attached to a pair of slightly modified standard MR headphones. The probes are located approximately on the vertices of a tetrahedron for well-conditioned field monitoring and position tracking.

Table 1
Gradient System Calibration Matrix

	Measured Responses							
	$\mathbf{G_x}$		$\mathbf{G_y}$		$\mathbf{G_z}$		$\mathbf{B_0}$	
Applied Tones	$\lvert\cdot\rvert$	Φ	$\lvert\cdot\rvert$	Φ	$\lvert\cdot\rvert$	Φ	$\lvert\cdot\rvert$	Φ
$\mathbf{G_x}$ (6 kHz)	**0.66**	−11°	$9.0{\cdot}10^{-4}$	(−147°)	$3.0{\cdot}10^{-3}$	(−75°)	$1.0{\cdot}10^{-2}$	(104°)
$\mathbf{G_y}$ (7 kHz)	$1.4{\cdot}10^{-3}$	(−62°)	**0.59**	−2°	$4.7{\cdot}10^{-4}$	(−103°)	$5.8{\cdot}10^{-3}$	(25°)
$\mathbf{G_z}$ (8 kHz)	$1.0{\cdot}10^{-3}$	(110°)	$1.4{\cdot}10^{-3}$	(−18°)	**0.53**	7°	$6.9{\cdot}10^{-3}$	(31°)

As expected, the magnitude ($\lvert\cdot\rvert$) of the desired field components (**bold**) decreases with increasing frequency. The coupling coefficients were determined with a magnitude precision between $1{\cdot}10^{-4}$ and $3{\cdot}10^{-4}$, and the magnitude-dependent phase (Φ) precision of the diagonal elements amounted to 0.014°. The phase precision of the low-magnitude off-diagonal elements was naturally lower and hence mentioned in brackets.

precision, and thus are placed in brackets. In order to compare contributions of field terms of different spatial orders, the elements were normalized such that they reflected field values on a sphere around the gradient isocenter with a diameter of 20 *cm*.

Performance of Probe Localization with Gradient Tones

The left-hand column of Figure 3 shows the SDs of the probe localization measurement and their theoretical predictions in the absence of sequence gradient activity. The gray horizontal lines denote the sample SD of the data points plotted by the green (x), red (y), and blue (z) dots. The shaded areas reflect predicted SD for each interleave (not of the measured sample). The measured SD amounted to 25 μm (x), 35 μm (y), and 41 μm (z). The predicted SDs were consistent with the measured ones and amounted to 24 μm (x), 31 μm (y), and 40 μm (z). The probe's SNR used for the predictions is illustrated at the top of Figure 3.

The right-hand column in Figure 3 shows both the measured (gray line) and the predicted (gray area) SD in the presence of the imaging sequence. As can be seen by the shape of the gray area and the probe's SNR at the top, the predicted sensitivity reflects the dependence on the applied phase encoding gradient, whose 0th-order moment defines the field probe's SNR, as illustrated at the top of Figure 3. Note that the measured precision reflects the sample's SD, whereas the gray area reflects the predicted SD for each time point. Also note that the sample noise is free of systematic errors that could have been induced, for example, by an incomplete separation between tones and sequence gradient waveforms.

Figure 4 shows the coordinates of the probe as it was moved from the start to the end position. The insets at the start position show very good agreement between the tones coordinates and the reference coordinates. The root-mean-square (RMS) and maximum (max) difference between the positions obtained with tones and the reference positions amounted to 33 μm (x, RMS), 151 μm (x, max), 33 μm (y, RMS), 233 μm (y, max), 42 μm (z, RMS), and 251 μm (z, max). The RMS difference between the two methods at the end position amounted to 583 μm (x, RMS), 771 μm (x, max), 595 μm (y, RMS), 822 (y, max) and 131 μm (z, RMS), and 358 μm (z, max). The RMS error of the coordinates at the end position computed with the simplified system model, which disregards both the off-diagonal elements of $\boldsymbol{C}$ and the vector $\boldsymbol{c}_0$, amounted to 480 μm (x), 2.53 *mm* (y), and 2.66 *mm* (z).

The subsequent experiment concerning the consistency of rigid-body parameters in the absence of motion yielded SDs of translation of 13 μm (x), 20 μm (y), and 25 μm (z), with maximal excursions of 55 μm (x), 83 μm (y), and 114 μm (z)—and SDs of rotation of 0.01° (x), 0.009° (y), and 0.01° (z), with maximal excursions of 0.031° (x), 0.025° (y), and 0.038°.

Motion Correction Experiments

Phantom Imaging

Figures 5a–c show the phantom in position 1, as obtained in the first phantom experiment. The image in Figure 5b was reconstructed with concurrently monitored dynamic field data and the image in Figure 5c with the reference trajectory. The result of the second phantom experiment is illustrated in Figures 5d,g. Figure 5d shows the image acquired without gradient tones, and Figure 5g shows its difference to the image acquired with tones, which is very minor in the range of a percent. The image artifacts induced by the tracking system are illustrated in Figure 5f, showing small artifacts at the edges and a clear image background with very subtle ghosting. Concurrent dynamic field monitoring reduces these artifacts, as illustrated in Figure 5e. The results from the fourth phantom experiment are illustrated in Figures 5i,k,m,n. Figure 5m shows the residual difference between the image data obtained at positions 1 and 2, with motion tracking and image reconstruction based on concurrent field monitoring. Figure 5n shows the same data but reconstructed with the reference trajectory. The residual differences in the order of a few percent reflect the changes in transmit and receive B_1 fields due to the altered geometric relationship between the phantom and the coils. The actual rotation of the setup amounted to approximately 11.2° and is illustrated in Figures 5h and l (difference image).

In Vivo Imaging

Figures 6a–b show the rotation and translation parameters observed in the in vivo experiment targeting in-plane rotation. The prescribed rotation around the magnet's main axis (z) is visible in the leftmost column.

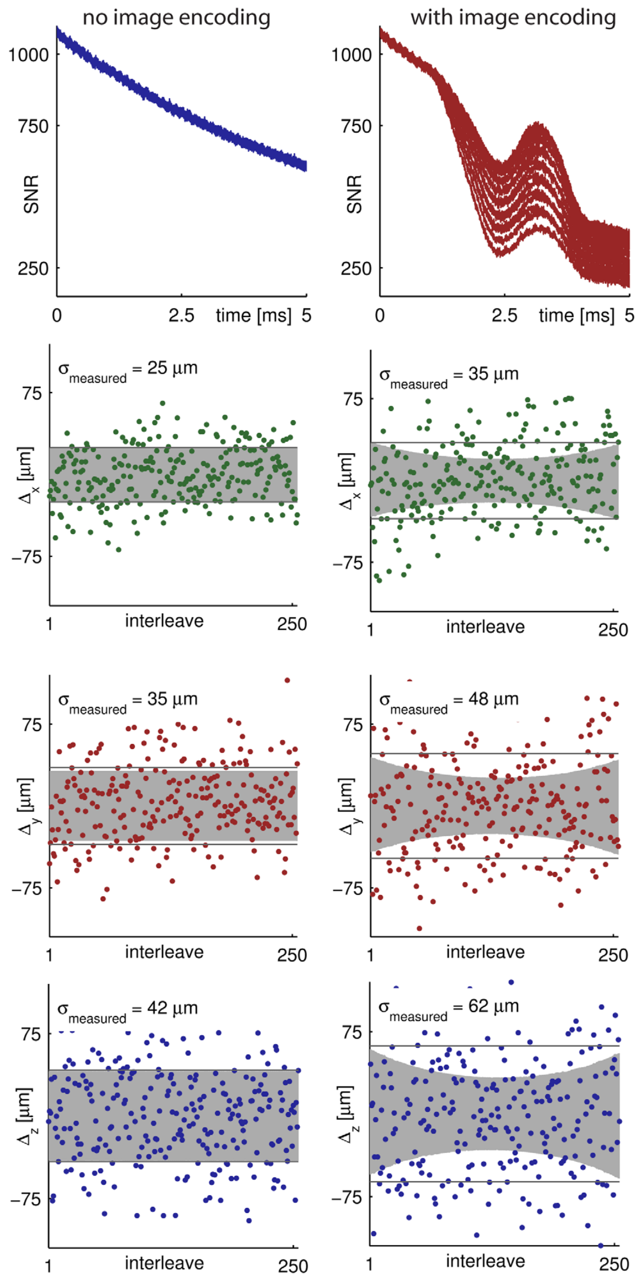

FIG. 3. **Left column:** Signal-to-noise ratio (SNR) (top) and sensitivity of tones-based probe localization without image encoding for the *x* (green), *y* (red), and *z* (blue) axis. The difference between the standard deviation of the sample and the prediction is below the figure's pixel resolution. The largest outliers are not shown due to scaling and amounted to 69 μm (*x*), 115 μm (*y*), and 129 μm (*z*). **Right column:** SNR and tones-based localization sensitivity during a spin-warp image encoding. The prediction (light gray) shows an interleave-dependence (interleaves 1 and 255 are farthest out in k-space; interleave 127 crosses the k-space center). The gradient system's transfer function renders the sensitivity frequency dependent, which is reflected in different precisions for each spatial dimension. The largest outliers in the right-hand column are not shown due to scaling and amounted to 111 μm (*x*), 220 μm (*y*), and 180 μm (*z*).

Translation along the *y*-axis shows that the prescribed head rotation was performed as a rolling motion, which is reflected in a rotation-correlated shift of the head's center of mass. Motion in the case where motion correction was applied is illustrated in Figure 6b and is in good agreement with both the prescribed rotation and the motion in the control experiment.

The right-hand side in Figure 6a shows the k-space trajectory of one slice, as monitored by the field probe array during the same experiments. The corresponding case with sequence update is illustrated in Figure 6b. Correction of the head motion by sequence update resulted in parallel phase encoding lines. It can further be seen that the tones amount to small deviations from the underlying Cartesian k-space sampling pattern, yet do not cause violations of the Nyquist sampling criterion throughout the k-space area used for image reconstruction. The slight compression of the tone pattern around $k_x = \pm\ 3.5\ rad/mm$ reflects ramping of the readout gradient.

Figures 6c–f show the resulting reconstructed images. Without correction all seven slices are corrupted by motion artifacts (Figs. 6c,d). Figures 6e and f show the effect of motion correction, which removed virtually all motion artifacts. There are no ghosting artifacts, which is reflected in the clear background of the scaled images. In the scaled images, residual blurring is still apparent at the edges of the head, and flow artifacts are visible along the phase-encoding direction. See Figure 7 for a close-up view of two selected slices.

For the in vivo experiment with deliberate translation, the observed Euler angles and translation are shown in Figures 8a,b. The prescribed shift along the magnet's main axis (*z*) is shown in the right-hand column of Figures 8a,b and amounted to $\pm 1\ cm$. The left-hand columns of Figures 8a,b illustrate that the shift was accompanied by a small correlated rotation around the *y*-axis (red graph). Motion in the corrected and the noncorrected case was in good agreement.

Figures 8c,d show image reconstructions for two slices without motion correction, again exhibiting severe motion

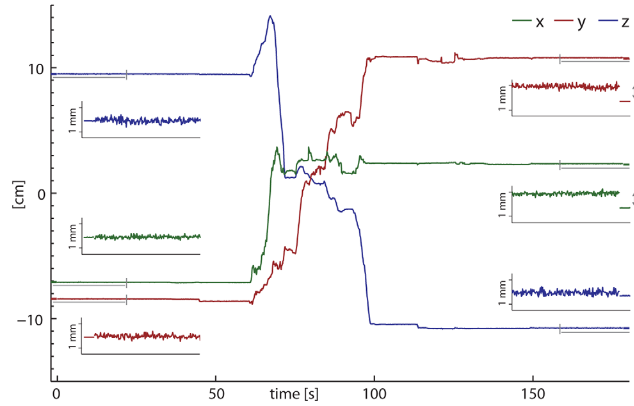

FIG. 4. Localization of a moving NMR field probe with gradient tones. The field probe was moved from a start position to an end position during a gradient tones sequence. At t = 0 s, the 20 reference position measurements, indicated in the close-up plots on the left-hand side, are consistent with the positions obtained with gradient tones. At the end position, at around t = 170 s, the discrepancy between the 20 reference position measurements and the tones-based positions amounts to 583 μm (*x*), 595 μm (*y*), and 131 μm (*z*), respectively. The insets illustrate data from the first 20 seconds (left-hand side) and last 20 seconds (right-hand side) of the experiment, respectively.

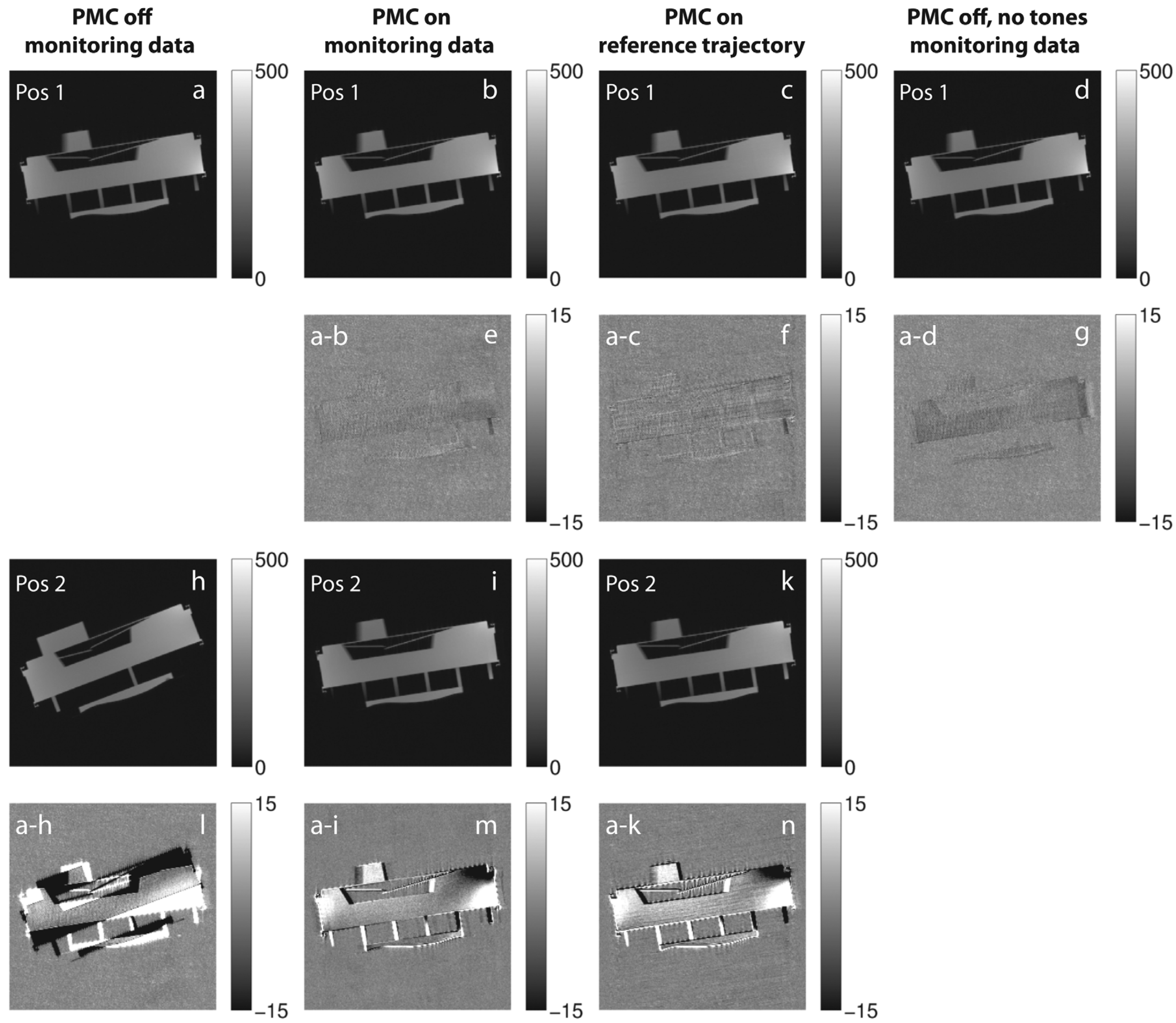

FIG. 5. Image reconstruction of the phantom experiments. (**a–c**) Image quality of the stationary phantom in position 1 without motion updates (a) and with motion updates with two different reconstruction methods (**b,c**). Difference images are shown in (**e,f**), illustrating the image artifacts induced by the tracking system (f), which is successfully corrected with field monitoring in the head frame (**e**). (**d,g**) Image reconstruction (d) and difference image (**g**) for an imaging readout without gradient tones, illustrating their effect on image quality. (**i,k,m,n**) Image reconstructions of the phantom in position 2 with motion correction with concurrent field monitoring-based (**i**) and reference–trajectory-based reconstruction (**k**). Corresponding difference images are shown in (**m,n**). A view of the phantom in position 2 is shown in (**h**), and the difference to the phantom in position 1 is shown in (**l**).

artifacts. Figures 8e and f, respectively, show the corresponding results with motion correction.

Figure 9 shows a comprehensive comparison of the different correction options. Figures 9a–d illustrate their effect on image quality for the prescribed in-plane rotation (top row). Figure 9a depicts a slice from the in-plane rotation experiment for which neither field monitoring nor prospective motion correction were applied. Figure 9b shows the same slice reconstructed with field monitoring data, which successfully corrects the in-plane motion. Figure 9c illustrates that prospective motion correction without field monitoring also yields a good result that was not further visibly improved by applying field monitoring, as illustrated in Figure 9d. The only visible difference between Figures 9c and d is a slight rotation, which is due to reconstruction in two different coordinate systems.

Figures 9e–h illustrate the effect of the different motion correction options in the experiment with prescribed through-plane motion. Figures 9e,f show that the image is corrupted by motion artifacts when no prospective motion correction is applied. Figure 9f illustrates that field monitoring alone is not effective at addressing through-plane motion. Figure 9g shows that prospective motion correction alone is effective at reducing the artifacts due to through-plane motion seen in Figure 9e; and Figure 9h, finally, shows the effect of additionally performing field monitoring, yielding no visible difference in image quality compared to Figure 9g. Again, as in Figures 9c,d, the only visible difference in Figures 9g,h is a rotation due to reconstruction in slightly different coordinate systems.

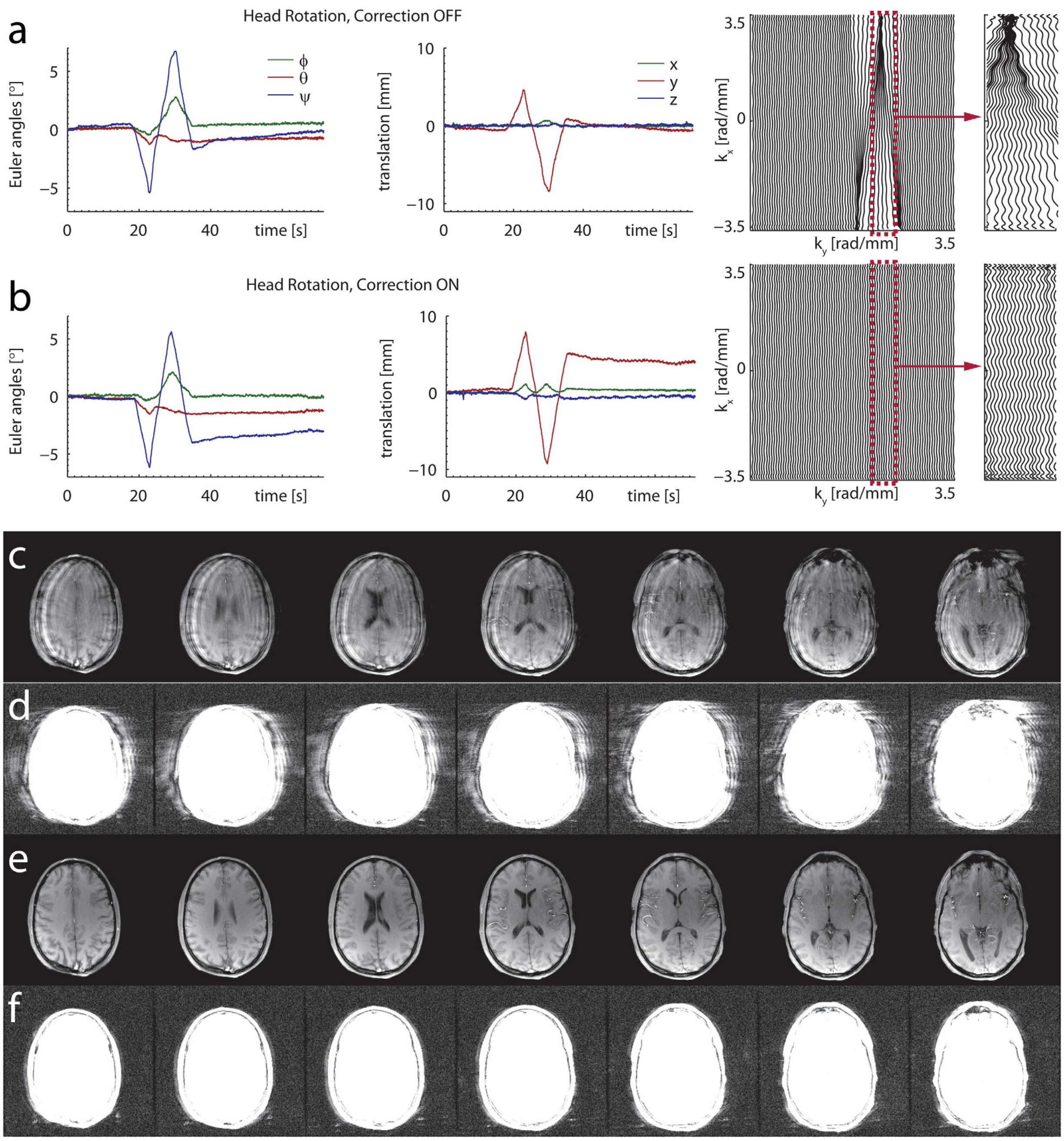

FIG. 6. (**a–b**) Euler angles and center of mass translation of the in vivo rotation experiment in the uncorrected case (first row) and in the motion-corrected case (second row). The rotation around the *z*-axis (blue graphs) was reproduced in both scans, and the shift along the *y*-axis (red graphs) shows that the prescribed head rotation was actually a rolling motion. The right-hand column shows the concurrently monitored k-space trajectory in the head frame of reference in the in vivo experiments. The overviews show the trajectory during the prescribed in-plane rotation where sequence update was performed (second row) and in the case of no update (first row). The close-ups show the amplitudes of gradient tones, which amounted to 0.5 Nyquist in the phase encode direction. In the motion-corrected case, subtle residual deviations from the reference trajectory resulted in slightly nonparallel encoding lines. In the uncorrected case, the rotation caused very strong distortions of the k-space sampling. The gradient trapezoid's ramp at the beginning and the end of each readout line causes denser sampling at the corresponding k-space positions. (**c–f**) Image reconstruction in the case of in-plane rotation. All seven slices are heavily corrupted by motion artifacts, as shown at both the linear (c) and the power scale (d). Tones-based slice tracking enables image reconstruction free of conspicuous motion artifacts (e); small residual artifacts are observed at the power scale (f).

DISCUSSION AND CONCLUSION

The results of this work show the successful implementation of gradient tones as a method to encode the position of NMR field probes, reaching precisions of 35 to 62 μm according to SDs observed in a stationary setup. The proposed solution enables the position tracking of field probes without any extra scan time and without line-of-sight access. Furthermore, it does not disturb the steady-state of the object under investigation. It is shown that the

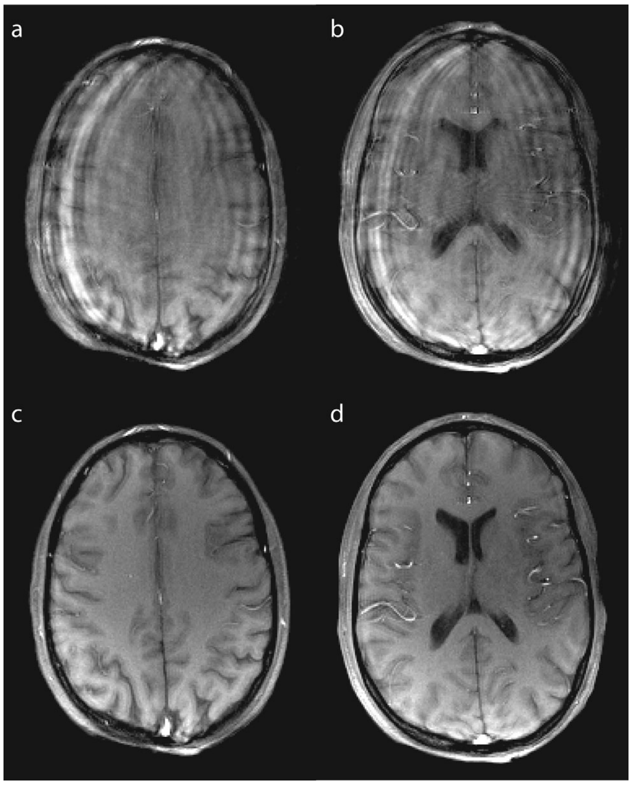

FIG. 7. Image reconstruction in the in-plane rotation experiment. Two out of seven slices are shown. In the uncorrected case (**a,b**), severe motion artifacts remain in the reconstructed image, whereas motion correction and field monitoring successfully remove them (**c,d**).

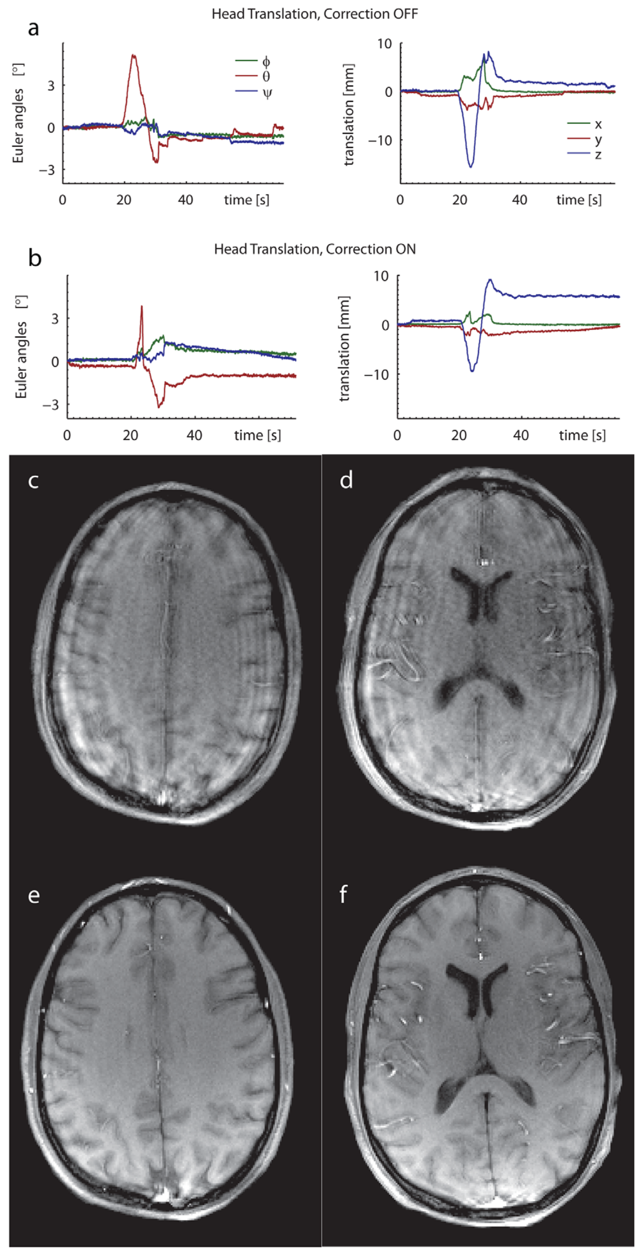

FIG. 8. (**a–b**) Euler angles and center of mass translation of the in vivo translation experiment in the uncorrected case (first row) and in the motion-corrected case (second row). The prescribed shift along the *z*-axis is very similar between the two experiments (right, blue graphs). The associated rotation around the *y*-axis (left, red graphs) refers to a subtle nodding motion during the shift. (**c–f**) Image reconstruction in the through-plane shift experiment. Two out of seven slices are shown. In the uncorrected case (c, d), severe motion artifacts remain in the reconstructed image, whereas motion correction and field monitoring successfully remove them (e, f).

combination of gradient tones and an array of four NMR field probes in a rigid body configuration allows synchronous real-time motion tracking and sequence monitoring in vivo. If desired, the 4-probe array used in this work allows for complementary field monitoring of 0th- and 1st-order dynamic fields in the head frame of reference.

These benefits come at the expense of additional hardware and software requirements. For this study, a suitable headset and transmit/receive hardware were built based on ^{19}F field probes and interfaced to a commercial spectrometer for concurrent ^{19}F and ^{1}H acquisition. Due to the proximity of ^{19}F and ^{1}H Larmor frequencies, such dual operation will amount to mere software changes on many receiver platforms. Nevertheless, it requires dedicating four receiver channels to the motion correction task. Add-on software was also written for the calculation of tone-enhanced gradient waveforms, for real-time probe-data analysis and sequence update, and for non-Cartesian image reconstruction based on field probe data.

The proposed method serves two purposes: It enables sequence update by encoding the head position and orientation in six degrees of freedom, and it optionally performs field monitoring in the head frame of reference. As shown in this work, field monitoring is inherently able to perform motion correction on its own if the motion is in-plane and causes only small Nyquist violations. With prospective motion correction, however, field monitoring did not visibly improve image quality. This suggests that undesired field perturbations and residual within-TR motion were negligible in the case studied. Field monitoring is expected to help, however, in applications where field perturbations of technical or physiological origin are significant. Problems of this kind have previously been described for anatomical imaging and fMRI at

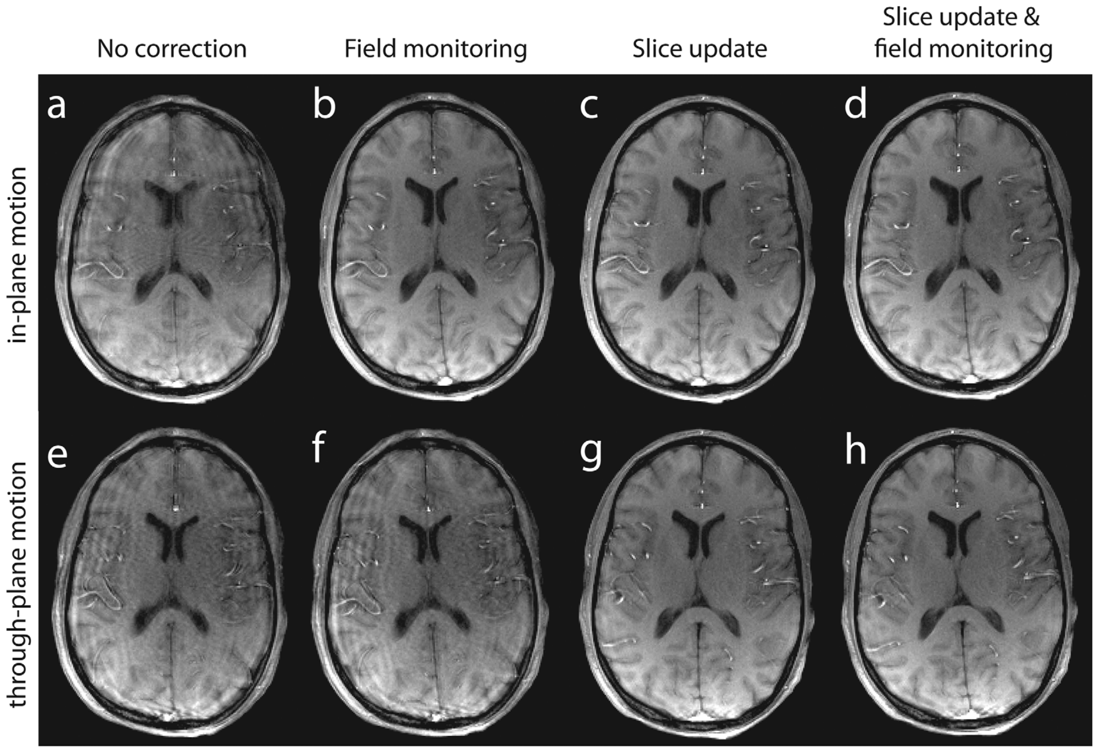

FIG. 9. Comparison of different motion correction methods. In-plane rotation (top row): (**a**) Severe image artifacts occur if neither field monitoring nor prospective motion correction are used. (**b**) Field monitoring alone successfully corrects for in-plane motion, which was also achieved by slice updates and image reconstruction with the reference trajectory (**c**). Field monitoring did not visibly improve image quality in the prospective motion correction experiment (**d**). Through-plane motion (bottom row): Severely corrupted image if no motion correction is used (**e**). Field monitoring alone is not able to correct for through-plane motion (**f**). Successful motion correction with tones-based sequence updates (**g**). Field monitoring did not further improve image quality in the motion correction experiment (**h**). The only visible differences between (c,d) and (g,h), respectively, are image rotations due to their reconstruction in different coordinate systems.

7T (37,38) and have successfully been accounted for with field monitoring (32,39–41).

The head setup used for head position tracking in this work relies on a rigid relation among the field probes and between the field probe array and the head, an issue that all current marker-based approaches have in common. In this work, we addressed it by designing the head setup to be both rigid and very light. It was operated without padding, which might have exerted confounding forces on the headset. For the presented method to be feasible, it was also important that the head coil used permitted suitable cable routing, which may require hardware integration in very dense, closed receiver arrays.

The frequency of the sequence update was locked to the sequence's TR and amounted to 25 Hz, sufficient for the bandwidth of the head motion present in this work. In order to embed prospective motion correction into sequences with shorter TR, the tracking can be decoupled from the sequence timing and the motion can be extrapolated. In order to encompass motion with higher bandwidth, the field probes will need to be re-excited after shorter time intervals and thus require a shorter T_1.

The moderate duty cycle of the sequence used in this work allowed both field monitoring for each readout and full T_1 recovery within one TR. However, sequences that offer no such benign duty cycle limit the application of field monitoring in the current implementation. A generic way of overcoming this limitation will be continuous field monitoring (42), which provides field monitoring completely independent of sequence duty cycle and timing.

The choice of the probe dimension (1-*mm* diameter), time window (4.8 *ms*), and image resolution (0.9 *mm*), as well as nominal tones amplitude (5 *mT/m*) and frequencies (6 *kHz*, 7 *kHz*, and 8 *kHz*, respectively) resulted in a localization precision of 35 to 62 μm. This is sufficient for typical applications that suffer from motion because of their target image resolution. Increased precision can be achieved according to the following trade-offs: If one chooses to boost probe SNR by increasing its diameter, the sensitivity will scale strongly with the probe diameter at a linear cost in maximum image resolution. Alternatively, one can choose to prolong the probe acquisition time and increase the sensitivity by a square root of time factor. Finally, one could increase the tones' localization power by scaling the nominal tones amplitude or decreasing their frequencies. Scaling up the gradient amplitudes causes a linear increase in sensitivity but comes at a linear expense of available gradient strength and slew rate available for image encoding. Decreasing the tones frequencies has several effects. It increases sensitivity according to the gradient impulse response function, whose magnitude response is relatively steep at the frequencies considered in this work (33). The results of the precision measurements showed a 44% increase (62 μm–35 μm) in precision when the frequency was reduced by 2 *kHz* (8 *kHz*–6 *kHz*). Also, lower tones frequencies increase the available slew rate for image encoding but also linearly increase the maximum k-space deviations from the underlying sampling pattern. Finally, the localization sensitivity will generally be somewhat reduced upon the onset of probe signal dephasing induced by image encoding gradients. It was found that the prediction of the position SD based on the probe's time-dependent SNR corresponded very well with measurements and may thus serve to roughly predict localization performance.

The results of the accuracy experiment show that the RMS localization error amounted to about 600 μm per axis for a position far away from calibration points, reflecting different possible model violations. One main reason is a discrepancy between gradient field shapes at the tones frequencies and zero frequency, respectively. The system response model used in this work considers field terms up to the first spatial order, but it has been previously shown that spatially nonlinear dynamic fields do occur (32). To address these, the higher-order tone field characterization could be incorporated in a calibration step involving more than the four positions. This would change the calibration model to one in which the measured tone response reflects a curvilinear coordinate system with coefficients that could be computed in the same way as for linear coordinates. Importantly, higher-order calibration would not affect the number of probes required in the headset. Gradient systems that are linear and time invariant will permit reusable one-time calibration. A second model violation is caused by concomitant fields. Negligible for high main field strengths as used in this work, it may become a relevant source of error at lower fields. Note, however, that it is possible to predict the concomitant fields to a high degree by using information about nominally known gradient waveforms. The extended field model resulting from these considerations will be nonlinear and will have to be addressed in future work.

A central aspect that also needs further investigation is the optimal embedding of probe localization capability into arbitrary gradient waveforms. In this work, sinusoidal tones were used because they permit simple response characterization, are robust against low frequency field contaminations, and can be placed in arbitrary time windows. Their placement is only limited by the practical need to avoid saturation of the probe receive chains during ^{1}H RF excitation and excessively fast probe dephasing, for example, during strong spoiler gradients. Tones are linearly independent, easy to orthogonalize, and of high power for high tracking precision within short time intervals. Also, if applied on top of an image-encoding gradient waveform, they impose small excursions on the k-space trajectory. Nonetheless, they need to be implemented such that these excursions are coordinated to avoid k-space gaps larger than the Nyquist limit. This was readily achieved in the sequence used in this work but may require further consideration in other cases. The separation between the sample sequence and the tones was rather straightforward because the former contained only small frequency components in the tones' frequency band. This situation will be different, for example, for spiral and EPI trajectories with substantial spectral content in the kilohertz range. For these, it is promising to use their native high-frequency components directly for probe localization, provided that they encompass sufficient energy for precise localization. To enhance sensitivity, it is conceivable to use entire frequency bands for localization, which will require additional considerations for calibration and signal processing.

ACKNOWLEDGMENT

Technical support by Philips Healthcare is gratefully acknowledged.

REFERENCES

1. Brown TT, Kuperman JM, Erhart M, White NS, Roddey JC, Shankaranarayanan A, Han ET, Rettmann D, Dale AM. Prospective motion correction of high-resolution magnetic resonance imaging data in children. Neuroimage 2010;53:139–145.
2. Ling J, Merideth F, Caprihan A, Pena A, Teshiba T, Mayer AR. Head injury or head motion? Assessment and quantification of motion artifacts in diffusion tensor imaging studies. Hum Brain Mapp 2012;33: 50–62.
3. Maclaren J, Armstrong BSR, Barrows RT, Danishad KA, Ernst T, Foster CL, Gumus K, Herbst M, Kadashevich IY, Kusik TP, et al. Measurement and correction of microscopic head motion during magnetic resonance imaging of the brain. PLoS One 2012;7:e48088.
4. Seto E, Sela G, McIlroy WE, Black SE, Staines WR, Bronskill MJ, McIntosh AR, Graham SJ. Quantifying head motion associated with motor tasks used in fMRI. Neuroimage 2001;14:284–297.
5. Schulz J, Siegert T, Bazin P-L, Maclaren J, Herbst M, Zaitsev M, Turner R. Prospective slice-by-slice motion correction reduces false positive activations in fMRI with task-correlated motion. Neuroimage 2014;84:124–132.
6. Speck O, Hennig J, Zaitsev M. prospective real-time slice-by-slice motion correction for fMRI in freely moving subjects. Magn Reson Mater Phy 2006;19:55–61.
7. Batchelor PG, Atkinson D, Irarrazaval P, Hill DLG, Hajnal J, Larkman D. Matrix description of general motion correction applied to multi-shot images. Magn Reson Med 2005;54:1273–1280.
8. Atkinson D, Hill DLG, Stoyle PNR, Summers PE, Clare S, Bowtell R, Keevil SF. Automatic compensation of motion artifacts in MRI. Magn Reson Med 1999;41:163–170.
9. Schmidt JFM, Buehrer M, Boesiger P, Kozerke S. Nonrigid retrospective respiratory motion correction in whole-heart coronary MRA. Magn Reson Med 2011;66:1541–1549.
10. Odille F, Vuissoz P-A, Marie P-Y, Felblinger J. Generalized Reconstruction by Inversion of Coupled Systems (GRICS) applied to free-breathing MRI. Magn Reson Med 2008;60:146–157.
11. Odille F, Uribe S, Batchelor PG, Prieto C, Schaeffter T, Atkinson D. Model-based reconstruction for cardiac cine MRI without ECG or breath holding. Magn Reson Med 2010;63:1247–1257.
12. Buerger C, Schaeffter T, King AP. Hierarchical adaptive local affine registration for fast and robust respiratory motion estimation. Med Image Anal 2011;15:551–564.
13. Filipovic M, Vuissoz P-A, Codreanu A, Claudon M, Felblinger J. Motion compensated generalized reconstruction for free-breathing dynamic contrast-enhanced MRI. Magn Reson Med 2011;65:812–822.
14. Nehrke K, Börnert P. Prospective correction of affine motion for arbitrary MR sequences on a clinical scanner. Magn Reson Med 2005;54: 1130–1138.
15. Lee CC, Jack CR, Grimm RC, Rossman PJ, Felmlee JP, Ehman RL, Riederer SJ. Real-time adaptive motion correction in functional MRI. Magn Reson Med 1996;36:436–444.
16. Lee CC, Grimm RC, Manduca A, Felmlee JP, Ehman RL, Riederer SJ, Jack CR. A prospective approach to correct for inter-image head rotation in FMRI. Magn Reson Med 1998;39:234–243.

17. Ehman RL, Felmlee JP. Adaptive technique for high-definition MR imaging of moving structures. Radiology 1989;173:255–263.
18. Fu ZW, Wang Y, Grimm RC, Rossman PJ, Felmlee JP, Riederer SJ, Ehman RL. Orbital navigator echoes for motion measurements in magnetic resonance imaging. Magn Reson Med 2005;34:746–753.
19. Van der Kouwe AJW, Benner T, Dale AM. Real-time rigid body motion correction and shimming using cloverleaf navigators. Magn Reson Med 2006;56:1019–1032.
20. Welch EB, Manduca A, Grimm RC, Ward HA, Jack Jr CR. Spherical navigator echoes for full 3D rigid body motion measurement in MRI. Magn Reson Med 2001;47:32–41.
21. Derbyshire JA, Wright GA, Henkelman RM, Hinks RS. Dynamic scan-plane tracking using MR position monitoring. J Magn Reson Imaging 1998;8:924–932.
22. Krueger S, Schaeffter T, Weiss S, Nehrke K, Rozijn T, Boernert P. Prospective intra-image compensation for non-periodic rigid body motion using active markers. In Proceedings of the 14th Annual Meeting of ISMRM, Seattle, Washington, USA, 2006. p. 3196.
23. Dumoulin CL, Souza SP, Darrow RD. Real-time position monitoring of invasive devices using magnetic resonance. Magnetic Resonance in Medicine 1993;29:411–415.
24. Ooi MB, Krueger S, Thomas WJ, Swaminathan SV, Brown TR. Prospective real-time correction for arbitrary head motion using active markers. Magn Reson Med 2009;62:943–954.
25. Ooi MB, Krueger S, Muraskin J, Thomas WJ, Brown TR. Echo-planar imaging with prospective slice-by-slice motion correction using active markers. Magn Reson Med 2011;66:73–81.
26. Zaitsev M, Dold C, Sakas G, Hennig J, Speck O. Magnetic resonance imaging of freely moving objects: prospective real-time motion correction using an external optical motion tracking system. Neuroimage 2006;31:1038–1050.
27. Aksoy M, Liu C, Moseley ME, Bammer R. Single-step nonlinear diffusion tensor estimation in the presence of microscopic and macroscopic motion. Magn Reson Med 2008;59:1138–1150.
28. Andrews-Shigaki BC, Armstrong BSR, Zaitsev M, Ernst T. Prospective motion correction for magnetic resonance spectroscopy using single camera retro-grate reflector optical tracking. J Magn Reson Imaging 2011;33:498–504.
29. Forman C, Aksoy M, Hornegger J, Bammer R. Self-encoded marker for optical prospective head motion correction in MRI. Med Image Anal 2011;15:708–719.
30. Barmet C, De Zanche N, Pruessmann KP. Spatiotemporal magnetic field monitoring for MR. Magn Reson Med 2008;60:187–197.
31. De Zanche N, Barmet C, Nordmeyer-Massner JA, Pruessmann KP. NMR probes for measuring magnetic fields and field dynamics in MR systems. Magn Reson Med 2008;60:176–186.
32. Wilm BJ, Barmet C, Pavan M, Pruessmann KP. Higher order reconstruction for MRI in the presence of spatiotemporal field perturbations. Magn Reson Med 2011;65:1690–1701.
33. Vannesjo SJ, Haeberlin M, Kasper L, Pavan M, Wilm BJ, Barmet C, Pruessmann KP. Gradient system characterization by impulse response measurements with a dynamic field camera. Magn Reson Med 2013;69:583–593.
34. Umeyama S. Least-squares estimation of transform parameters between two point patterns. IEEE Trans Pattern Anal Mach Intell 1991;13:376–380.
35. Barmet C, Wilm B, Pavan M, Katsikatsov G, Keupp J, Mens G, Pruessmann KP. Concurrent higher-order field monitoring for routine head MRI: an integrated heteronuclear setup. In Proceedings of the 18th Annual Meeting of ISMRM, Stockholm, Sweden, 2010. p. 216.
36. Barmet C, De Zanche N, Wilm BJ, Pruessmann KP. A transmit/receive system for magnetic field monitoring of in vivo MRI. Magn Reson Med 2009;62:269–276.
37. Versluis MJ, Peeters JM, van Rooden S, van der Grond J, van Buchem MA, Webb AG, van Osch MJP. Origin and reduction of motion and f0 artifacts in high resolution T2*-weighted magnetic resonance imaging: application in Alzheimer's disease patients. Neuroimage 2010; 51:1082–1088.
38. Van de Moortele P-F, Pfeuffer J, Glover GH, Ugurbil K, Hu X. Respiration-induced B0 fluctuations and their spatial distribution in the human brain at 7 Tesla. Magn Reson Med 2002;47:888–895.
39. Vannesjo SJ, Wilm B, Duerst Y, Gross S, Brunner DO, Dietrich BE, Schmid T, Barmet C and Pruessmann KP. Retrospective correction of physiological field fluctuations in high-field brain MRI using concurrent field monitoring. Magn Reson Med 2015;73:1833–1843.
40. Kasper L, Bollmann S, Vannesjo SJ, Gross S, Haeberlin M, Dietrich BE, Pruessmann KP. Monitoring, analysis, and correction of magnetic field fluctuations in echo planar imaging time series. Magn Reson Med 2015;74:396–409.
41. Kasper L, Haeberlin M, Dietrich BE, Gross S, Barmet C, Wilm BJ, Vannesjo SJ, Brunner DO, Ruff CC, Stephan KE, Pruessmann KP. Matched-filter acquisition for BOLD fMRI. Neuroimage 2014;100C: 145–160.
42. Dietrich B, Barmet C, Brunner D, Pruessmann KP. An Autonomous System for Continuous Field Monitoring with Interleaved Probe Sets. In: Proceedings of the 19th Annual Meeting of ISMRM, Montréal, Canada, 2011. p. 1842.